Large Dendritic Monolayer MoS_2 Grown by Atmospheric Pressure Chemical Vapor Deposition for Electrocatalysis

*Wenshuo Xu,[†] Sha Li,[†] Si Zhou,[†] Ja Kyung Lee,[†] Shanshan Wang,[†] Syed Ghazi Sarwat,[†] Xiaochen Wang,[†] Harish Bhaskaran,[†] Mauro Pasta,[†] Jamie H. Warner[†]**

[†]Department of Materials, University of Oxford, Parks Road, Oxford, OX1 3PH, United Kingdom

*Jamie.warner@materials.ox.ac.uk;

KEYWORDS: MoS_2, catalyst, monolayer dendrites, hydrogen evolution reaction (HER), chemical vapor deposition (CVD)

ABSTRACT: The edge sites of MoS_2 are catalytically active for the hydrogen evolution reaction (HER) and growing monolayer structures that are edge rich is desirable. Here, we show the production of large-area highly branched MoS_2 dendrites on amorphous SiO_2/Si substrates using an atmospheric pressure chemical vapour deposition (APCVD) and explore their use in electrocatalysis. By tailoring the substrate construction, the monolayer MoS_2 evolves from triangular to dendritic morphology due to the change of growth conditions. The rough edges endow dendritic MoS_2 with a fractal dimension down to 1.54. Highly crystalline basal plane and edge of the dendrites are visualized at atomic resolution using ADF-STEM. The monolayer dendrites exhibit strong photoluminescence (PL), indicative of the direct band gap emission, which is preserved after being transferred. Post-transfer sulfur annealing restores the structural defects and decreases the n-type doping in MoS_2 monolayers. The annealed MoS_2 dendrites

show good and highly durable HER performance on glassy carbon with a large exchange current density of 32 μA cm^{-2}_{geo}, demonstrating its viability as an efficient HER catalyst.

INTRODUCTION

MoS_2 is a layered material with promising catalytic behavior toward hydrogen evolution reaction (HER).[1–6] The electrocatalytic activity typically occurs at edge sites of MoS_2 and at defects of sulfur atoms (*i.e.*, unsaturated states and vacancies).[2–5,7–10] Metallic 1T-phase MoS_2 normally displays superior HER performance compared with semiconducting 2H-phase because of the additional reactive sites across the basal planes that are electrochemically inert for 2H-MoS_2,[4,11,12] and further improvement can thus be achieved through a phase transition from 2H to 1T.[13,14] The catalytic activity of 2H-MoS_2 increases linearly with the number of edge sites,[7] whereas it decreases linearly with the layer number due to the reducing electron hopping efficiency.[15] Alternative ways to increase the HER catalysis of MoS_2 include chemical doping and defect/strain engineering, which modulate the lattice structure and electronic states,[2,3,16–23] and hybridizing with other materials.[24–32]

There are a variety of methods to produce MoS_2 for electrocatalysis, such as electrochemical intercalation,[33] chemical exfoliation,[11,12] solvothermal reaction,[34] and chemical vapour deposition (CVD).[6,35–37] Improving the catalytically active CVD grown thin films of MoS_2 usually centers around enriching the edge numbers, for example, by growing vertically aligned films or porous structures with exposed edges.[4,6,13,38–40] Monolayer MoS_2 that is effective for HER can also be obtained by CVD,[41,42] provided that the films are not fully continuous and are instead composed of numerous isolated flakes that have abundant edges. Controlling the CVD growth parameters to achieve dendritic shaped MoS_2 domains increases the number of catalytic sites relative to areal coverage.[41,43]

Although it has been reported that the morphology of monolayer MoS_2 is variable by modifying the heated temperature and carrier gas flow rate in CVD,[41,44,45] the change in domain

shape is constricted within a narrow range and the lateral size is small. Few-layer dendritic MoS_2 has been synthesized in a previous study by changing the carrier gas flow rate in the CVD process,[43] while the photoluminescence (PL) of these dendrites is significantly weaker compared to their monolayer counterparts because of the indirect band gap.[46] Low pressure CVD (LPCVD) has been adopted to grow dendritic MoS_2 monolayers on a single crystal substrate of $SrTiO_3$ (STO (100)), but the domain size is limited to ~10 μm, and high coverage has not been achieved simultaneously with the increase in branching degree,[41] which restricts the density of active edge sites. Therefore, further work on producing highly fractal MoS_2 is of interest to for enhanced HER efficiency, especially for CVD-grown MoS_2.

In this study we utilize a three-stage APCVD technique to synthesize highly uniform monolayer MoS_2 dendrites on amorphous SiO_2/Si substrates with large domain size. The ambient condition ensures a facile and green synthesis with lower reaction temperature and simplified experimental equipment. Each aspect of the CVD process can be controlled individually and allows the growth of large monolayer domains. The flake evolves from triangular to highly dendritic shape by customizing our home-built substrate. The electrochemical catalytic behaviors of these large-area MoS_2 with different crystal morphologies are characterized on glassy carbon. We explore the effects of transfer and sulfur annealing on the PL and HER performance of monolayer MoS_2, which also grant us the ability to investigate the sole contribution of edges to the HER activities.

RESULTS AND DISCUSSION

Figure 1a depicts the atmospheric pressure chemical vapor deposition used in the present work for growing monolayer MoS_2. Large-area MoS_2 nanosheets are produced by a three-stage growth (Figure 1b). Sufficient precursor feedstocks are provided by a high gas flow rate during the

initial stage to form nuclei. After that the main growth starts under a lower gas flow rate, and proceeds by consuming the excess precursors at local sites. Then the gas flow rate is further decreased so that the atoms residing on the domain surfaces can migrate freely to the adjacent edges. The temperature is simultaneously decreased in order to reduce both the feedstock of MoO_3 and the sublimation of as-produced MoS_2.

The relative concentrations of the gaseous precursors vary greatly on different substrate surfaces. The atom ratio of Mo:S can determine the shape of the resulting MoS_2 domains.[37] Herein monolayer MoS_2 flakes with various morphologies are controllably synthesized in a single growth by adjusting the position of the substrate chips. The low Mo:S ratio on the bottom substrate typically gives rise to MoS_2 dendrites with a high branching degree (Figure 1d and f), whereas normal triangular MoS_2 crystals are grown at the same time on the other three substrates (Figure 1c and e). Figure 1f presents an abundance of edge sites accommodated by the dendritic pattern. As the growth system is rich in sulfur, the nucleation density of MoS_2 relies on the concentration of MoO_3, which is very low in close proximity to the tube wall. Lateral growth is favored at the nuclei with lower densities, giving a larger domain size of the dendritic MoS_2 on the bottom substrate. The optimized CVD procedure and substrate construction allow the production of large-area, highly dendritic MoS_2 monolayers with the arm length up to ~390 μm.

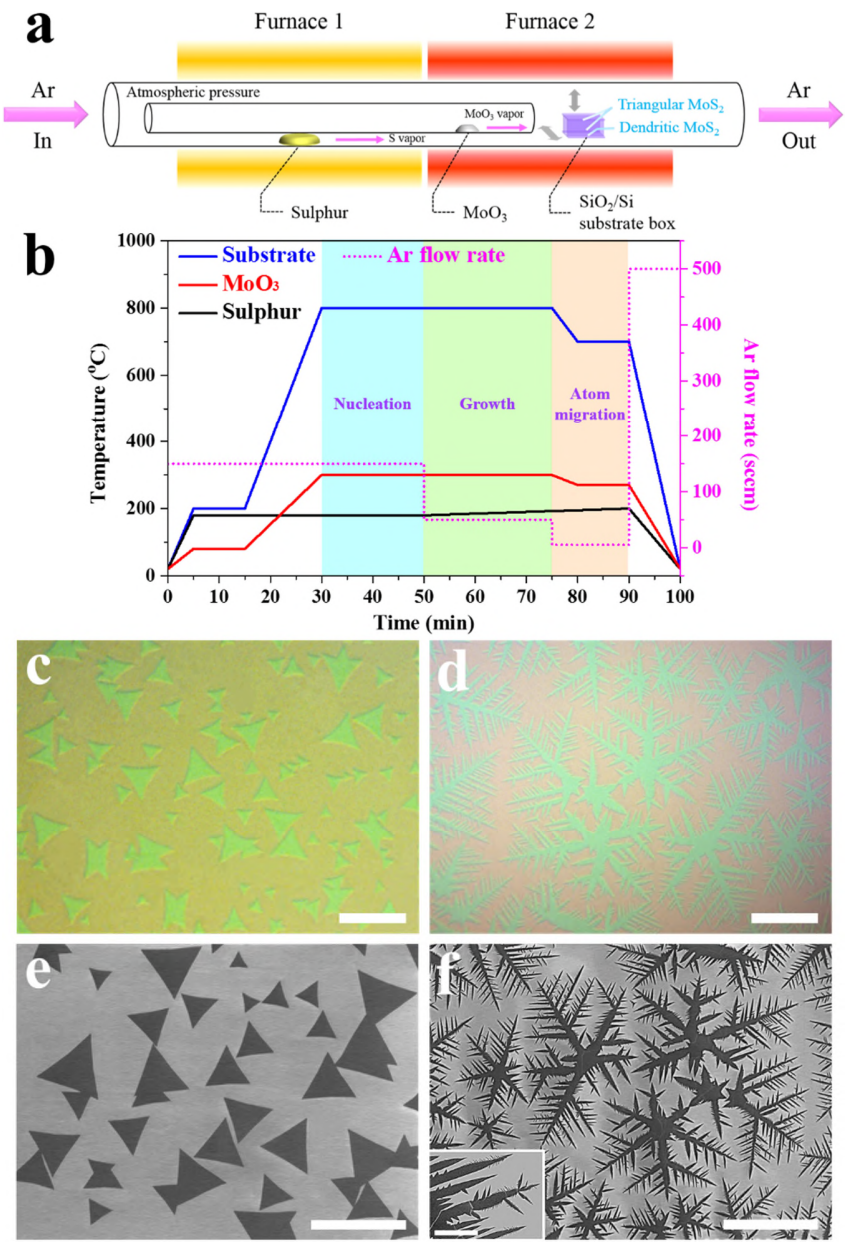

Figure 1. (a) CVD setup for the synthesis of MoS_2 domains. (b) Profiles of the temperature and carrier gas flow rate programmed for the formation of large-area MoS_2 monolayer flakes with varied morphologies. (c, d) Optical microscope images and (e, f) SEM images for the as-grown triangular and dendritic MoS_2, respectively. Scale bar: 200 µm. The inset of panel f shows the fine detail of a dendrite tip; scale bar: 10 µm.

The shape of the MoS_2 domain is also tunable by altering the distance of the SiO_2/Si chip to the gas flow. The branching degree is dependent on the local ratio of Mo:S, which is in turn determined by the location of the substrate surfaces.[37] The construction of the self-supported substrate box is flexibly tailorable. The inside and outside chips can be shifted along the directions indicated with the grey arrows in Figure 1a, and the top chip can be moved up or down while changing the width of the side chips (perpendicular to the gas line). Figure 2a illustrates the spatial concentration of the sulfur vapor, which is affected by both the distance to the source (radial degradation) and the distance along the quartz tube (linear degradation) because of the temperature gradient in the furnaces. Taking the bottom chip as an example, Figure 2a also indicates how this substrate is controllably located to attain the evolving domain morphologies in Figure 2b−i. It is notable that the growth on the bottom substrate is independent of the presence of the other three. Since the temperature of the SiO_2 surfaces is kept identical, the Mo:S ratio is dependent on and sensitive to the height of the substrate (green arrow). When reducing the chip width (blue arrows), the substrate is closer to the inside wall of the quartz tube at a lower height, where the concentration ratio of Mo:S is smaller. It is found that larger relative concentration of the sulfur results in a higher branching degree of the MoS_2 products. The shape evolution is noticeable with a decrease of every 2.0 ± 0.5 mm in width, from 2 cm for strictly triangular MoS_2 (Figure 2b) to 0.6 cm for highly dendritic MoS_2 (Figure 2i). Further narrowing the substrate would cause insufficient feeding of the precursors, and scale down the macroscopic area of the sample. The branched monolayer MoS_2 in Figure 2e–i contain a large density of grain boundaries, and hence are likely to show distinct optical and electrical properties.[47]

The complexity and roughness of the fractal pattern is of interest because it is correlated to the HER activities of MoS_2. It can be evaluated by the fractal dimension of the crystal pattern.

Box-counting method is usually applied for the calculation, based on the number of boxes touching the domain edges as a function of scaling factor.[48] The fractal dimension for monolayer MoS_2, indicated by the slope of the linear regression, increases from 1.15 (triangular outline, Supporting Information Figure S1a) to 1.54 (highly dendritic outline, Supporting Information Figure S1h). This demonstrates that through the adjustment of substrate construction, the edge of MoS_2 is increasingly rough with the shape change, therefore holding potential for enhanced HER performance.

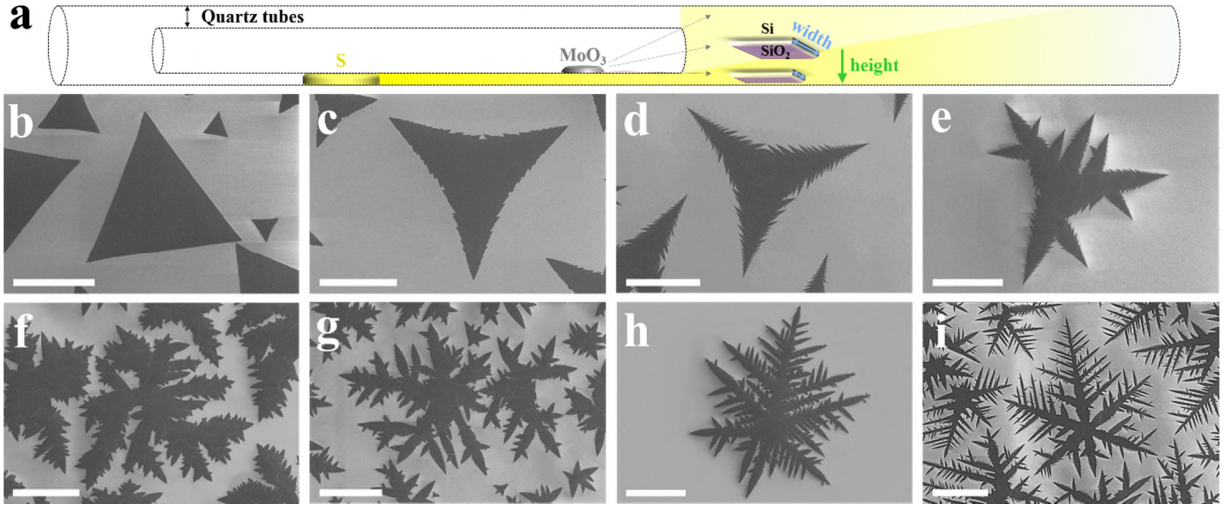

Figure 2. Shape evolution of the as-synthesized MoS_2 on bottom SiO_2/Si substrate. (a) Schematic diagram of the substrate positioning relative to the precursor vapors. (b−i) SEM images of the resulting monolayer MoS_2. The domain evolves from the normal triangular shape in panel b to the highly dendritic shape in panel i. Scale bar: 100 μm.

The higher flux of sulfur vapor around the bottom substrate triggers a growth transition from thermodynamic mode to kinetic mode. The precursor molecules attach to the existing crystal with the anomalous diffusion of precursors, and the growth is preferred along the lowest-energy diffusion paths on the substrate, instead of the crystal edges,[49] so that the islands develop into

large fractal-like structures (Figure 2i). Unlike crystalline substrates such as $SrTiO_3$,[50] where the preferential diffusion paths are specified and restricted by the well-organized surface structures, highly anisotropic surface energies are offered by the amorphous SiO_2/Si substrate. This could promote the branching along directions concurrent with the expansion of domain area, leading to dendritic large MoS_2 islands. A moderate precursor flux results in thermodynamic growth, and at equilibrium triangular MoS_2 flakes are produced (Figure 3a). In another case, the growth mode could switch intermittently near the transition threshold, and accordingly, the MoS_2 grows laterally *via* the attachment of precursor molecules along domain edges (under thermodynamic control) while shooting out arms along the crystal facets (under dynamic control). By virtue of this combined regime, branched structures are generated with more compact body, wider arms, and less hierarchical morphology relative to the sharp dendrites (Figure 3c). The determination of growth mode is highly sensitive to the concentrations of precursor vapors at specific locations, which explains the feasibility of achieving various branching degrees. The configurations of the as-grown MoS_2 are carefully inspected in Figure 3, where each hierarchal level is indicated by one arrow color. For either side of the arms, the offshoots and side sprouts show parallel alignments, respectively. However, the offshoots in any hierarchical level grow forward away from the central core/axis, while the side sprouts grow backward pointing to the main body. Interestingly, the angles measured by the arm axes are all ~60° between the primary backbones and the secondary arms (I & II), the secondary and the tertiary arms (II & III), the tertiary and the quaternary arms (III & IV), as well as the side sprouts and their affiliated arms (SS and A), regardless of their positions (*e.g.*, Figure 3b). The results are summarized in Figure 3f, with the error bars <8.2%. We also observed three-fold symmetric backbones for the triangular domains and six-fold symmetric backbones for the dendrites, both centered at the nucleation core.

Therefore the growth mechanism in our scenario cannot be interpreted purely by the classical diffusion-limited aggregation (DLA) model giving random dendritic configurations.[51] Since certain lattice directions are energetically favorable (*e.g.*, zigzag or armchair direction) at the growth front, backbones would prefer to develop from the nucleation core with symmetries, and similarly, side branches tend to form a 60° angle to the arm at deflection sites when the growth is driven by kinetics. This could apply to other TMD materials with the same low-energy pathways.

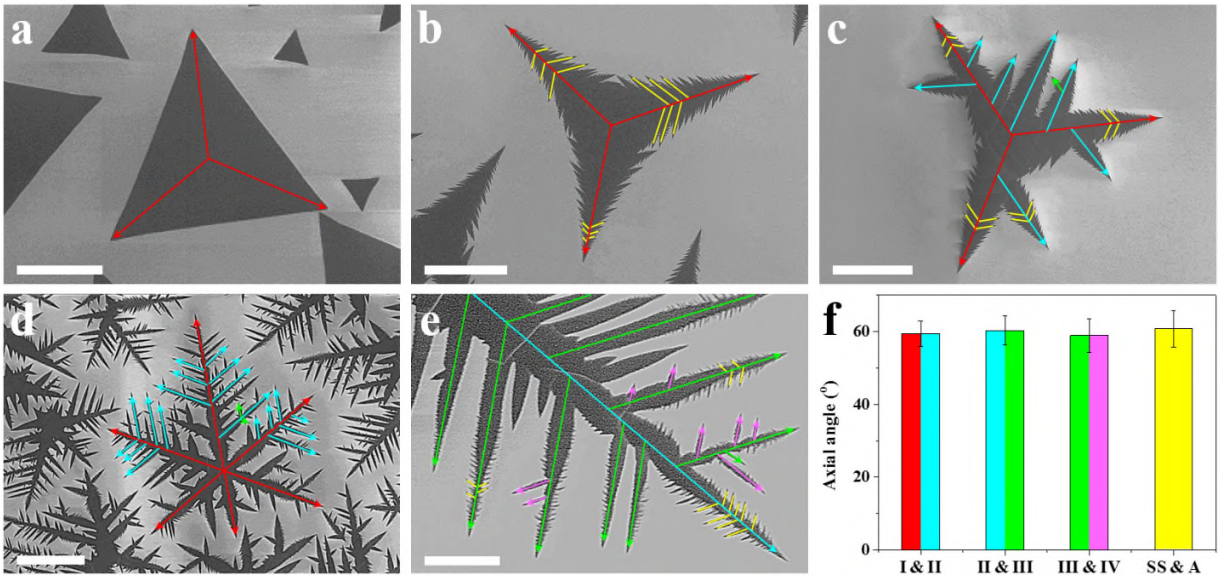

Figure 3. Analysis of the CVD-grown monolayer MoS_2 with (a) strict triangular, (b) star triangular, (c) branched, and (d) highly dendritic morphologies. The hierarchical structures are marked by arrows, *i.e.*, red for the primary (I) backbone, cyan, green, and pink for the secondary (II), tertiary (III), and quaternary (IV) arms. The side sprouts (SS) are marked by yellow lines. (f) Histogram of the axial angle between different hierarchical arms (I and II, II and III, III and IV), and between the arms and their side sprouts (SS and A). The first three columns are bi-colored according to the hierarchy levels of the arms, consistent with panel a–e, while considering the high similarities, the results for the side sprouts affiliated with arms II to IV are generalized in the yellow column. Scale bar: (a–d) 100 μm for panel; (e) 20 μm.

The low magnification ADF-STEM images in Figures 4a and b show a small dendritic shaped domain of MoS_2. The atomic resolution ADF-STEM images in Figure 4c and d are from typical dendritic MoS_2 samples and show the high crystallinity of the material. The hole in the inset of Figure 4d was induced *in situ* by focused electron beam irradiation (>5 min),[52] which reveals that the MoS_2 is monolayer. The dendrite edges in Figure 4e–h indicate that the domain has zigzag edge terminations in both S and Mo directions, which is expected due to the presence of six arm branches from the core of the dendrite. For both the basal plane and the edge of the dendritic MoS_2 monolayer, the hexagonal atomic arrangements are the same as that of the triangular and truncated triangular shaped MoS_2,[10,53] demonstrating identical crystal lattice at the nanoscale despite the change in crystal morphologies.

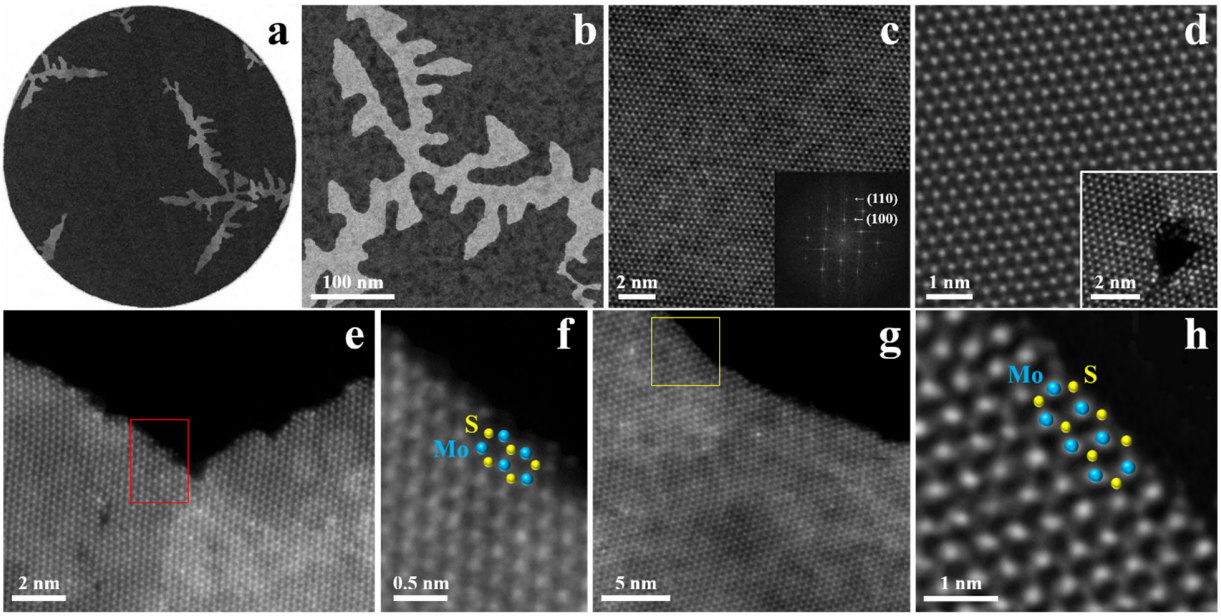

Figure 4. (a, b) ADF-STEM images of the MoS_2 dendrites under lower magnification. (c) Atomic resolution ADF-STEM image of a dendritic MoS_2 monolayer with the corresponding FFT pattern as an inset and (d) a higher magnified image with the result after prolonged irradiation as an inset. The dendrite edges under (e, g) lower magnification and (f, h) higher magnification of the red and yellow boxed

regions in panel e and g, respectively, showing that the edge termination is either a Mo (e, f) or an S (g, h) zigzag direction.

Raman and PL spectroscopy were performed to explore the physical properties of the MoS_2 grown on SiO_2/Si substrates. Figure 5a shows the two characteristic Raman modes of MoS_2, E^1_{2g} (~384.0 cm^{-1}) and A_{1g} (~403.6 cm^{-1}). The E^1_{2g} mode corresponds to the in-plane Mo−S phonon and is preferentially excited for terrace terminations, whereas the A_{1g} mode corresponds to the out-of-plane Mo−S phonon and is preferentially excited for edge terminations. The relative intensities between A_{1g} and E^1_{2g} can therefore provide information on the texture of MoS_2.[6,39] For both triangular and dendritic domains, the integrated intensity ratios of A_{1g}/E^1_{2g} ~1 conform well to the reported value of monolayer MoS_2,[54] indicating that terrace sites are predominant in the nanosheets.[39] However, the dendritic MoS_2 shows a slightly higher A_{1g}/E^1_{2g} ratio, which is suggestive of a rougher surface. Strong PL is observed in these monolayers (Figure 5b),[55] and the PL intensities are comparable of both morphologies. It is noteworthy that the PL intensity and peak position have minor deviations (intensity ± 5.4%; peak position ± 3.6%), mainly due to the temperature profile in the CVD furnaces for centimeter-scale synthesis,[56] which are yet negligible (intensity ± 0.8%; peak position ± 0.5%) within single domains. We further extract the quantitative information about the as-grown MoS_2 dendrites in Figure 5c by fitting the data to Gaussian functions with three peaks originating from B exciton, A exciton, and A^- trion. The neutral excitons of A and B arise from two different transitions within the direct band gap of monolayer MoS_2, whereas the A^- trion is a bound state of two electrons and one hole (namely, A exciton + a free electron) *via* Coulomb interactions due to the n-type doping from charged SiO_2 surfaces.[57] The Raman and PL maps in Figure 5e−g and j−l show the integrated intensity and

peak position over the energy range corresponding to the peaks in the Raman (Figure 5a) and PL spectra (Figure 5b), and verify that our CVD-grown MoS_2 is highly uniform. The frequency difference between A_{1g} and E^1_{2g} modes can be used to precisely determine the layer number of MoS_2, and the values lying within the range of 18.5−19.0 cm^{-1} confirm the monolayer nature across the domains (Figure 5h and m).[54] The thicknesses are also confirmed by AFM measurements (Supporting Information Figure S2).

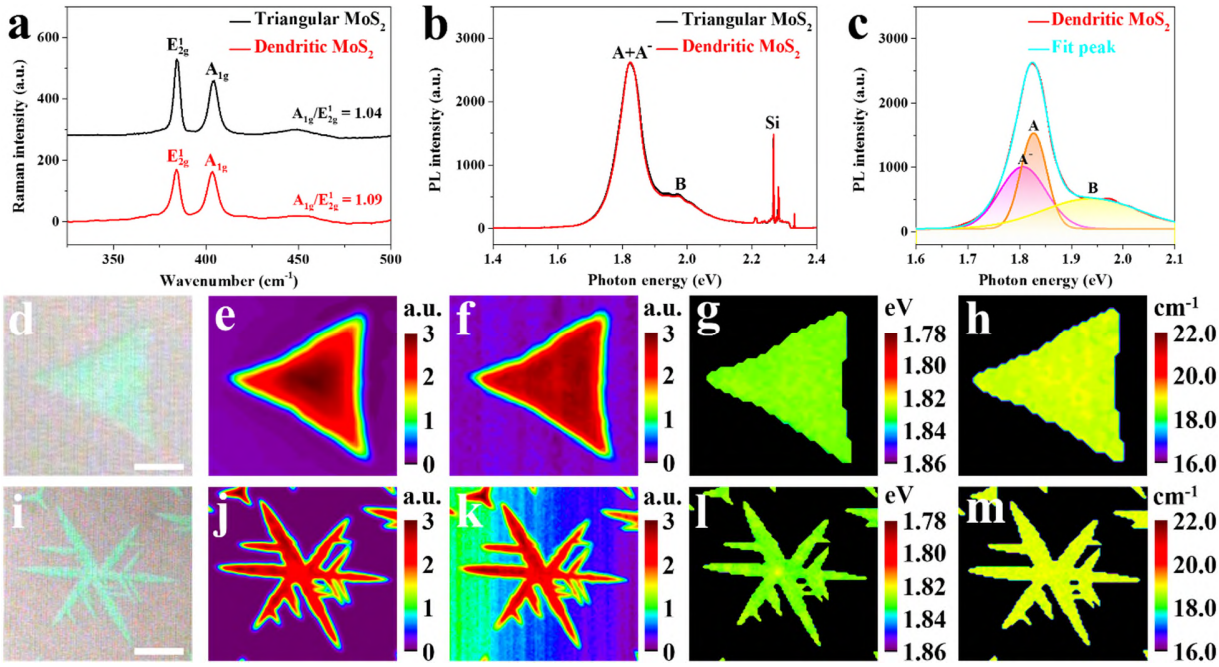

Figure 5. Raman and PL studies of the as-grown MoS_2 on SiO_2/Si substrates. (a) Raman and (b) normalized PL spectra of the triangular MoS_2 and dendritic MoS_2. (c) Deconvoluted PL spectrum of the dendritic MoS_2 with Gaussian fitting (PL components: B exciton, A exciton, and A^- trion). (d, i) Optical microscope images of triangular MoS_2 and dendritic MoS_2 for measurements. Total (e, j) PL and (f, k) Raman integrated intensities, (g, l) PL peak positions, and (h, m) frequency differences between A_{1g} and E^1_{2g} Raman peaks of (e−h) triangular and (j−m) dendritic MoS_2. Scale bar: 30 μm.

Nanostructured MoS_2 is an active electrocatalyst for HER. The catalytic response was found to correlate linearly with the number of edge sites.[7] Therefore dendritic MoS_2 is promising to exhibit improved HER performance in comparison with other monolayer morphologies. We transferred the CVD-grown MoS_2 onto conductive glassy carbon as the working electrode in the HER. Figure 6a and b show the as-transferred triangular and dendritic MoS_2 flakes on glassy carbon. The electrocatalytic activities of MoS_2 depend on several factors, including the phase,[4,11,12] layer number,[15] structural disorders,[2–5,9,10] and strain,[2,3,16] apart from the density of edge sites.[4–8] 2H phase MoS_2 is produced by CVD method, and the inbuilt strain is released through a wet transfer process. The release of strain is evidenced by comparing the PL spectra of the dendritic MoS_2 grown on SiO_2/Si substrate (red curves in Figure 5b and c), with that transferred to glassy carbon (purple curves in Figure 6c and e). The PL peak position is blue-shifted by 17.1 meV (6.3 nm) after the transfer, which corresponds to ~0.27% strain for MoS_2 monolayers.[58] Monolayer MoS_2 exhibits the optimal catalytic performance due to the high electron hopping efficiency, which decreases significantly with more layers added.[15] However, sulfur vacancies are inevitably generated during the transfer. Therefore the individual contribution of edge sites to the catalytic efficiency can be analyzed only if the influences of defects are minimized. To this end, we conduct thermal annealing for the transferred MoS_2 in sulfur vapor environment. The PL of the MoS_2 dendrites is probed before and after annealing. It is found that the PL intensity is increased (Figure 6c) and the peak width is narrowed together with a red shift (Figure 6d) after the annealing treatment. Figure 6e and f present the detailed Gaussian fits before and after annealing, respectively. The enhanced PL peak intensity suggests that the crystallinity of MoS_2 is improved.[10] Besides, the annealing results in less localized states (LS), which are associated with defects such as sulfur vacancies.[59] The change in peak intensity

ratio of A/A^- reflects the varied relative population density of excitons and trions.[57] The increased A/A^- ratio after the annealing indicates a reduced concentration of electrons in the material. These observations show that sulfur atoms have been incorporated into the crystal lattice of MoS_2 during the annealing process. It fills the sulfur vacancies, and causes p-type doping in the MoS_2 nanosheets. However, it should be mentioned that defects cannot be entirely restored so that the LS peak of annealed sample is still not negligible in the Gaussian fitting.

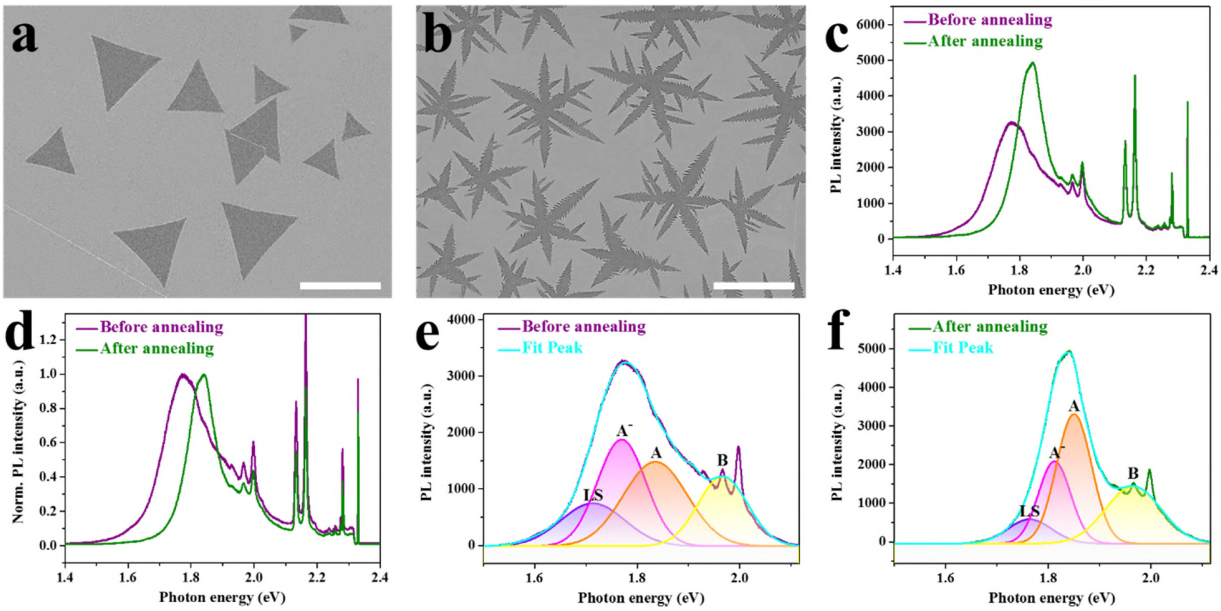

Figure 6. SEM images of the as-transferred (a) triangular MoS_2 and (b) dendritic MoS_2 on glassy carbon plates. (c) PL spectra and (d) normalized PL spectra before (purple curves) and after (green curves) annealing. (e, f) Deconvoluted PL spectra using Gaussian fitting into four PL components, *i.e.*, B exciton, A exciton, A^- trion and localized states (LS). Scale bar: 30 μm.

Pre-cycling could be necessary for transferred monolayer MoS_2 to reach stabilities according to previous work,[5] and this has been done prior to our electrochemistry measurements (Supporting Information Figure S3). The MoS_2 was not grown directly on glassy carbon substrates as the smoother surface of SiO_2 is beneficial to high uniformity and large-scale synthesis, especially for

2D monolayers.[57,60] The LSV results in Figure 7a indicates that the dendritic MoS_2 displays an enhancement of the HER activities with increased current density (j or j_{geo}), and the performances are even improved after one thousand times cycling. A sensible interpretation could be that the existing sulfur vacancies tend to aggregate and proliferate in the strained structure during the cycling process,[61] by which the active site density is increased inside the basal plane of the 2H-MoS_2. However, the HER performance then degrades rapidly upon further cycling. In contrast, the MoS_2 exhibits high durability after the transfer and sulfur annealing, though lower HER activities are observed initially (Figure 7d). This is owning to the successful elimination of the strained sulfur vacancies, which are unstable reactive sites in the MoS_2 monolayers. A long-term cycling test up to 30 thousand times was applied to the branched MoS_2, and proves the excellent stability of the post-annealed MoS_2 monolayers. The MoS_2 dendrites also show a lower Tafel slope (Figure 7b and e), suggesting that lower overpotential would be required for a certain increase in current density. As largely influenced by the strain in sulfur vacancies,[3] the Tafel slope increases after the transfer and annealing treatments, indicating reduced HER efficiencies, while it was little relevant to the domain coverage if annealed in H_2S atmosphere.[7] Additionally, the difference in Tafel slopes is smaller between the dendritic and triangular MoS_2 after sulfur annealing, which could result from the exclusion of strained sulfur vacancies associated with domain edges. Exchange current density (j_0) is used to describe the efficiency of electron transfer in catalysts at zero overpotential (η). It can be calculated by fitting the linear portion of the Tafel plot ($\log j$ *vs.* η) at large values of η.[7,62] A large exchange current density of 37 μA cm^{-2}_{geo} is reached by the as-transferred (*i.e.*, non-annealed) dendritic MoS_2 incorporating plentiful strained sulfur vacancies, while the annealing-derived highly crystalline MoS_2 with much less structural defects shows an exchange current density of 32 μA cm^{-2}_{geo} for

the dendrites, and 14.5 μA cm^{-2}_{geo} and 0.8 μA cm^{-2}_{geo} for the branched and triangular structures, respectively. Full details about the calculation of exchange current densities are presented in Supporting Information S4. These values match well with the literature regarding HER (0.13–38.9 μA cm^{-2}_{geo}), and the behavior of our highly crystalline dendrites is among the best reported for monolayer MoS_2 catalysts that were not engineered to be integrally defective or heterostructured with other materials, irrespective of morphologies, substrates, and preparation methods.[2,6,7,34,38,39,41,63−67] The larger exchange current densities were attributed to the massive amount of active catalyst materials in the bulk MoS_2 compared to the monolayers we have grown and/or the substantial defects that were deliberately incorporated.[2,21,64] The exchange current density of MoS_2 has also been increased beyond 38.9 μA cm^{-2}_{geo} *via* hybridizations.[25,31] Considering that the areal coverage of the MoS_2 dendrites is 12% higher due to the large domain size, as determined by the SEM images in Figure 1e and f, the exchange current density of the dendritic MoS_2 is ~37 times larger than that of the triangular counterpart. Electrochemical impedance spectroscopy (EIS) is also employed to analyze the catalytic property of the MoS_2, shown in Figure 7c and f. The semi-arc curve at low frequency region is an indicator of the kinetic control in the electrode process, and any mass transfer control is excluded, consistent with other studies,[4,5,41] which would otherwise give an additional straight line with 45° angle at low frequency region. It is revealed by the smaller radius of the semi-arc that dendritic morphology with significantly increased edge density permits a decreased charge transfer resistance (R_{ct}) across the MoS_2–electrolyte interface. This can facilitate the rate-determining step in the HER, *i.e.*, proton discharge (Volmer reaction: $H_3O^+ + e^- \rightarrow H_{ads} + H_2O$) in our case, and thereby improve the catalytic activity of MoS_2.[68] As the *x*-axis intercept at high frequency region represents the ohmic impedance of the reaction system,[69] the dendrites show a lower

electrical resistance (R_s), in agreement with the larger areal coverage (a) of 12% based on Ohm's Law ($R = \rho\, l\, a^{-1}$, where ρ is identical for polycrystalline MoS_2 and is l the fixed monolayer thickness). Moreover, the sulfur annealing for either domain shape leads to a slightly higher R_s, stemming from the reduction in sulfur vacancies that act as n-dopants in MoS_2. Figure 7g–i link the edge density (E_D) with the HER behavior. The change from triangular to highly dendritic domain shape corresponds to an increase in E_D, whereby the HER performance of monolayer MoS_2 is enhanced. The exchange current density and onset potential correlate almost in a linear fashion with E_D (Figure 7g and i, respectively). The trend of j_0 *vs.* E_D is similar to that in earlier studies.[7,10] However, the decrease in Tafel slope is more obviously smaller at high E_D (Figure 7h), as it relies on the Volmer reaction whose rate consistently limits these HER processes.

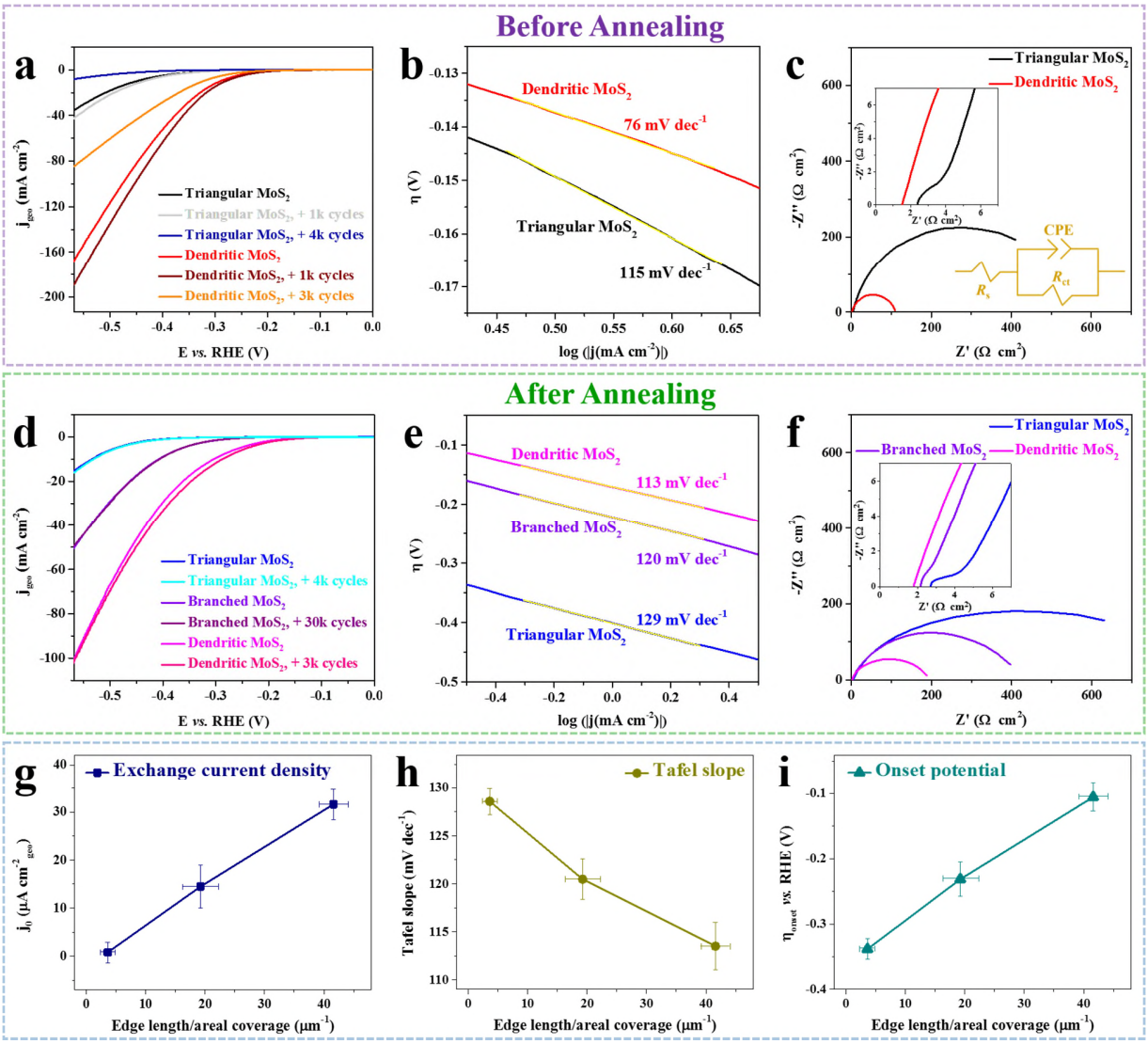

Figure 7. HER activities of the triangular and highly dendritic MoS_2 on glassy carbon plates (a–c) before annealing and (d–f) after annealing. (a, d) Cathodic polarization curves with cycling procedures applied. (b, e) Tafel plots with the slopes obtained *via* linear fits. (c, f) Nyquist plots at 10 mV, indicating the impedance of the electrochemical system, with the insets zoomed in at the high frequency region and an equivalent circuit in panel c. Correlations of edge length density (E_D = edge length/areal coverage) with the (g) exchange current density, (h) Tafel slope, and (i) onset potential. The HER activities are normalized to the geometric area of the working electrode (glassy carbon plates), denoted by the subscript

of 'geo', and the edge length densities are calculated with respect to the domain area to exclude the influences of coverage variations.

CONCLUSION

In summary, our results show the large-area synthesis of uniform MoS_2 monolayer dendrites on amorphous SiO_2/Si substrates by a three-stage APCVD growth. The domain shape is controllable *via* precise design of the substrates. The highly dendritic MoS_2 possesses a low fractal dimension of 1.54 associated with its rough edges. The MoS_2 dendrites derive from a DLA-like process, while its backbones have six-fold symmetry and the side branches are well aligned ~60° to the arms because of the preferential growth along certain low-energy directions. Direct gap PL emission is observed in the monolayer MoS_2 both before and after the transfer onto glassy carbon. Annealing the MoS_2 in sulfur atmosphere contributes to high crystallinity by reducing the defect level as well as n-type doping. The large density of catalytically reactive sites enables the dendritic MoS_2 to deliver outstanding HER performance and long-term electrochemical stability after defect restoration.

EXPERIMENTAL SECTION

APCVD Synthesis of Monolayer MoS_2. The monolayer MoS_2 domains were grown by hydrogen-free APCVD with the precursors of molybdenum trioxide (MoO_3, powder, ≥99.5%, Sigma-Aldrich) and sulfur (S, powder, ≥99.5%, Sigma-Aldrich). P-doped silicon (Si) coated with a 300 nm thick oxide layer (SiO_2) was used as the substrate. After being sonicated for 10–15 min in acetone and isopropanol solution successively, 4 pieces of the SiO_2/Si substrates (2 cm × 1 cm) were cemented together to build a cuboid box with all the SiO_2 surfaces facing out. We employed double-walled quartz tubes for the CVD synthesis to avoid cross-reaction between the precursors.[37] Two separate furnaces were utilized for individual temperature control. The MoO_3 (15 mg) loaded in the inner tube (0.6 inch diameter) was placed in the central zone of Furnace 1,

and the S (600 mg) in the outer tube (1 inch diameter) was placed 1.7 cm from the left open end of Furnace 2; the SiO_2/Si substrate box was located at the center of Furnace 2, as shown in Figure 1. The growth system was first flushed with 500 sccm argon (Ar) for 30 min to drive off the oxygen. Then the furnaces were ramped to ~180 °C and ~200 °C, respectively, so as to create a sulfur-rich environment. Next, Furnace 2 was heated up to 800 °C, and in the meanwhile, the temperature of MoO_3 was increased to 300 °C. Once the target temperature was reached, the MoS_2 began to nucleate with 150 sccm Ar flow. This stage lasts for 20 min, after which the flow rate was reduced to 50 sccm for a 25 min growth. The temperature of S was increased slowly from 180 °C to 200 °C since then to maintain the concentration of S vapor at a nearly constant level. The growth time could be extended to 39 min in order to obtain bilayer dendrites, with the second-layer islands located on top of the large-area dendritic monolayer. To attain high uniformity and large domain size, we for the first time designed a follow-up procedure that enabled atom migrations, where the MoO_3 temperature was reduced to 270 °C and the gas flow rate was dropped to 5 sccm for a lower precursor feedstock, with a quenched substrate temperature of 700 °C to decrease the sublimation of MoS_2 species formed on the substrates. The time for obtaining large domain size was optimized to be 15 min. Finally, the synthesis ended up with fast cooling.

Transfer of the CVD-Synthesized MoS_2. The as-grown MoS_2 sample was first spin-coated with a thin film of poly(methyl methacrylate) (PMMA, 8 wt% in anisole, 495k molecular weight) at 4500 rpm for 60 s, followed by a 90 s curing process at 180 °C. The SiO_2 layer was etched off by floating the sample on a 1 M potassium hydroxide (KOH, Sigma-Aldrich) aqueous solution in 50 °C water bath, when the planar strain in the MoS_2 nanosheets was released. The isolated film of PMMA/MoS_2 was then rinsed in deionized (DI) water three times for 1 h each.

Sequentially, a piece of glassy carbon (Sigma-Aldrich) pre-cleaned using the aforementioned procedure for SiO_2/Si substrates, or a TEM grid (a supported 200 nm thick Si_3N_4 film perforated by an array of 2 μm diameter viewing holes, Agar Scientific Y5358), was submerged into the DI water to fish the film. The as-transferred sample was left overnight in a ventilation environment. When the water was totally dried, we baked the sample at 150 °C for 25 min to enhance the interface adhesion. The complete removal of PMMA was achieved by 2 steps. Firstly, the sample was soaked in a 55 °C acetone bath for 48 h, where most of the PMMA was dissolved. Subsequently, we annealed the sample in the presence of S vapor both to remove the remaining PMMA residue and to fill the S vacancies. In this process the S powder (150 mg) and the sample were sealed in a quartz tube and were positioned at the centers of two furnaces, similar to the CVD growth. After the system had been flushed by 500 sccm Ar flow for 30 min, the furnaces were ramped up to 200 °C and 270 °C, respectively. The S vapor was then transported with 300 sccm Ar flow downstream to the sample for 60 min. This was followed by a slow cooling process to avoid the formation of strain.

Characterization. The MoS_2 samples were imaged at room temperate utilizing optical microscope, scanning electron microscope (SEM, Hitachi-4300, 3.0 kV accelerating voltage), and annular dark field scanning transmission electron microscope (ADF-STEM, JEOL ARM-200F STEM with a CEOS aberration corrector, 80 kV accelerating voltage). Dwell times of 32 μS and a pixel size of 0.0073−0.015 nm px^{-1} were applied for the ADF-STEM imaging, along with a 30 μm CL aperture, 24.6 mrad convergence semiangle, 12 pA beam current, and 39−156 mrad inner acquisition angle. The ADF-STEM images were subjected to a Gaussian smooth. Raman and PL spectroscopy were carried out with a JY Horiba LabRAM ARAMIS imaging confocal Raman microscope. A 12.5 mW, 532 nm (2.33 eV) diode laser was employed for

excitation, which was focused down to a ~1 μm spot. The acquisition time for spectra and maps was 1 s and 0.1 s, respectively. Atomic force microscope (AFM) was used to measure the layer thickness by Asylum Research MFP-3D in AC mode with a silicon AC-160TS cantilever (Olympus, spring constant of ~42 N m^{-1} and resonant frequency of ~300 kHz).

Electrochemical Measurements. The catalytic performance of the CVD-grown MoS_2 was tested in a three-electrode system, using the monolayer MoS_2 transferred on glassy carbon as the working electrode, a Pt wire (or alternatively, carbon rod, in Supporting Information S5) as the counter electrode, and Ag/AgCl/ KCl (3 M) as the reference electrode. A defined working area of the sample was immerged into a 0.5 M H_2SO_4 N_2-purged solution for HER activities. The potentials were calibrated to a reversible hydrogen electrode (E (RHE) = E (Ag/AgCl/ KCl (3 M)) + 0.21 − 0.059·pH). Cyclic voltammetry (CV) was applied at a scan rate of 100 mV s^{-1} to clean the sample surface till the current signal kept stable.[5] Then linear sweep voltammetry (LSV) was conducted under quasi-equilibrium conditions at 1 mV s^{-1}. Electrochemical impedance spectroscopy (EIS) was measured by sweeping the frequency from 200000 Hz to 1 Hz with a perturbation voltage amplitude of 10 mV.

ASSOCIATED CONTENT

Supporting Information

The Supporting Information is available free of charge on the ACS Publications website.

Calculation of the fractal dimension, AFM measurements, ADF-STEM imaging of the transferred MoS_2 with sulfur vacancies, pre-cycling treatments for the HER, calculation of the exchange current density, effects of the counter electrode on HER activities, and ADF-STEM imaging of second-layer MoS_2 dendrites grown on top of the dendritic monolayer domain

ACKNOWLEDGMENTS

J.H.W. thanks the Royal Society for support.

REFERENCES

(1) Yan, Y.; Xia, B.; Xu, Z.; Wang, X. Recent Development of Molybdenum Sulfides as Advanced Electrocatalysts for Hydrogen Evolution Reaction. *ACS Catal.* **2014**, *4*, 1693–1705.

(2) Li, H.; Tsai, C.; Koh, A. L.; Cai, L.; Contryman, A. W.; Fragapane, A. H.; Zhao, J.; Han, H. S.; Manoharan, H. C.; Abild-Pedersen, F.; Nørskov, J. K.; Zheng, X. Activating and Optimizing MoS_2 Basal Planes for Hydrogen Evolution through the Formation of Strained Sulphur Vacancies. *Nat. Mater.* **2016**, *15*, 48–53.

(3) Li, H.; Du, M.; Mleczko, M. J.; Koh, A. L.; Nishi, Y.; Pop, E.; Bard, A. J.; Zheng, X. Kinetic Study of Hydrogen Evolution Reaction over Strained MoS_2 with Sulfur Vacancies Using Scanning Electrochemical Microscopy. *J. Am. Chem. Soc.* **2016**, *138*, 5123–5129.

(4) Yin, Y.; Han, J.; Zhang, Y.; Zhang, X.; Xu, P.; Yuan, Q.; Samad, L.; Wang, X.; Wang, Y.; Zhang, Z.; Zhang, P.; Cao, X.; Song, B.; Jin, S. Contributions of Phase, Sulfur Vacancies, and Edges to the Hydrogen Evolution Reaction Catalytic Activity of Porous Molybdenum Disulfide Nanosheets. *J. Am. Chem. Soc.* **2016**, *138*, 7965–7972.

(5) Li, G.; Zhang, D.; Qiao, Q.; Yu, Y.; Peterson, D.; Zafar, A.; Kumar, R.; Curtarolo, S.; Hunte, F.; Shannon, S.; Zhu, Y.; Yang, W.; Cao, L. All the Catalytic Active Sites of MoS_2 for Hydrogen Evolution. *J. Am. Chem. Soc.* **2016**, *138*, 16632−16638.

(6) Li, S.; Wang, S.; Salamone, M. M.; Robertson, A. W.; Nayak, S.; Kim, H.; Tsang, S. E.; Pasta, M; Warner, J. H. Edge-Enriched 2D MoS_2 Thin Films Grown by Chemical Vapor Deposition for Enhanced Catalytic Performance. *ACS Catal.* **2017**, *7*, 877–886.

(7) Jaramillo, T. F.; Jørgensen, K. P.; Bonde, J.; Nielsen, J. H.; Horch, S.; Chorkendorff, I. Identification of Active Edge Sites for Electrochemical H_2 Evolution from MoS_2 Nanocatalysts. *Science* **2007**, *317*, 100–102.

(8) Xie, J.; Zhang, H.; Li, S.; Wang, R.; Sun, X.; Zhou, M.; Zhou, J.; Lou, X. W. D.; Xie, Y. Defect-Rich MoS_2 Ultrathin Nanosheets with Additional Active Edge Sites for Enhanced Electrocatalytic Hydrogen Evolution. *Adv. Mater.* **2013**, *25*, 5807–5813.

(9) Xie, J.; Zhang, J.; Li, S.; Grote, F.; Zhang, X.; Zhang, H.; Wang, R.; Lei, Y.; Pan, B.; Xie, Y. Controllable Disorder Engineering in Oxygen-Incorporated MoS_2 Ultrathin Nanosheets for Efficient Hydrogen Evolution. *J. Am. Chem. Soc.* **2013**, *135*, 17881–17888.

(10) Ye, G.; Gong, Y.; Lin, J.; Li, B.; He, Y.; Pantelides, S. T.; Zhou, W.; Vajtai, R.; Ajayan, P. M. Defects Engineered Monolayer MoS_2 for Improved Hydrogen Evolution Reaction. *Nano Lett.* **2016**, *16*, 1097–1103.

(11) Lukowski, M. A.; Daniel, A. S.; Meng, F.; Forticaux, A.; Li, L.; Jin, S. Enhanced Hydrogen Evolution Catalysis from Chemically Exfoliated Metallic MoS_2 Nanosheets. *J. Am. Chem. Soc.* **2013**, *135*, 10274–10277.

(12) Voiry, D.; Salehi, M.; Silva, R.; Fujita, T.; Chen, M.; Asefa, T.; Shenoy, V. B.; Eda, G.; Chhowalla, M. Conducting MoS_2 Nanosheets as Catalysts for Hydrogen Evolution Reaction. *Nano Lett.* **2013**, *13*, 6222–6227.

(13) Wang, H.; Lu, Z.; Xu, S.; Kong, D.; Cha, J. J.; Zheng, G.; Hsu, P.-C.; Yan, K.; Bradshaw, D.; Prinz, F. B.; Cui, Y. Electrochemical Tuning of Vertically Aligned MoS_2 Nanofilms

and Its Application in Improving Hydrogen Evolution Reaction. *Proc. Natl. Acad. Sci.* **2013**, *110*, 19701–19706.
(14) Kang, Y.; Najmaei, S.; Liu, Z.; Bao, Y.; Wang, Y.; Zhu, X.; Halas, N. J.; Nordlander, P.; Ajayan, P. M.; Lou, J.; Fang, Z. Plasmonic Hot Electron Induced Structural Phase Transition in a MoS_2 Monolayer. *Adv. Mater.* **2014**, *26*, 6467–6471.
(15) Yu, Y.; Huang, S.-Y.; Li, Y.; Steinmann, S. N.; Yang, W.; Cao, L. Layer-Dependent Electrocatalysis of MoS_2 for Hydrogen Evolution. *Nano Lett.* **2014**, *14*, 553–558.
(16) Lee, J. H.; Jang, W. S.; Han, S. W.; Baik, H. K. Efficient Hydrogen Evolution by Mechanically Strained MoS_2 Nanosheets. *Langmuir* **2014**, *30*, 9866–9873.
(17) Deng, J.; Li, H.; Xiao, J.; Tu, Y.; Deng, D.; Yang, H.; Tian, H.; Li, J.; Ren, P.; Bao, X. Triggering the Electrocatalytic Hydrogen Evolution Activity of the Inert Two-Dimensional MoS_2 Surface *via* Single-Atom Metal Doping. *Energy Environ Sci.* **2015**, *8*, 1594–1601.
(18) Wang, H.; Tsai, C.; Kong, D.; Chan, K.; Abild-Pedersen, F.; Nørskov, J. K.; Cui, Y. Transition-Metal Doped Edge Sites in Vertically Aligned MoS_2 Catalysts for Enhanced Hydrogen Evolution. *Nano Res.* **2015**, *8*, 566–575.
(19) Dai, X.; Du, K.; Li, Z.; Liu, M.; Ma, Y.; Sun, H.; Zhang, X.; Yang, Y. Co-Doped MoS_2 Nanosheets with the Dominant CoMoS Phase Coated on Carbon as an Excellent Electrocatalyst for Hydrogen Evolution. *ACS Appl. Mater. Interfaces* **2015**, *7*, 27242–27253.
(20) Ren, X.; Ma, Q.; Fan, H.; Pang, L.; Zhang, Y.; Yao, Y.; Ren, X.; Liu, S. A Se-Doped MoS_2 Nanosheet for Improved Hydrogen Evolution Reaction. *Chem. Commun.* **2015**, *51*, 15997–16000.
(21) Xie, J.; Qu, H.; Xin, J.; Zhang, X.; Cui, G.; Zhang, X.; Bao, J.; Tang, B.; Xie, Y. Defect-Rich MoS_2 Nanowall Catalyst for Efficient Hydrogen Evolution Reaction. *Nano Res.* **2017**, *10*, 1178–1188.
(22) Ray, C.; Lee, S. C.; Sankar, K. V.; Jin, B.; Lee, J.; Park, J. H.; Jun, S. C. Amorphous Phosphorus-Incorporated Cobalt Molybdenum Sulfide on Carbon Cloth: Efficient and Stable Electrocatalyst for Enhanced Overall Water Splitting over Entire pH Values. *ACS Appl. Mater. Interfaces* **2017**, *9*, 37739–37749.
(23) Chen, Y.-C.; Lu, A.-Y.; Lu, P.; Yang, X.; Jiang, C.-M.; Mariano, M.; Kaehr, B.; Lin, O.; Taylor, A.; Sharp, I. D.; Li, L.-J.; Chou, S. S.; Tung, V. Structurally Deformed MoS_2 for Electrochemically Stable, Thermally Resistant, and Highly Efficient Hydrogen Evolution Reaction. *Adv. Mater.* **2017**, 1703863.
(24) Li, Y.; Wang, H.; Xie, L.; Liang, Y.; Hong, G.; Dai, H. MoS_2 Nanoparticles Grown on Graphene: An Advanced Catalyst for the Hydrogen Evolution Reaction. *J. Am. Chem. Soc.* **2011**, *133*, 7296–7299.
(25) Firmiano, E. G. S.; Cordeiro, M. A. L.; Rabelo, A. C.; Dalmaschio, C. J.; Pinheiro, A. N.; Pereira, E. C.; Leite, E. R. Graphene Oxide as a Highly Selective Substrate to Synthesize a Layered MoS_2 Hybrid Electrocatalyst. *Chem. Commun.* **2012**, *48*, 7687−7689.
(26) Liao, L.; Zhu, J.; Bian, X.; Zhu, L.; Scanlon, M. D.; Girault, H. H.; Liu, B. MoS_2 Formed on Mesoporous Graphene as a Highly Active Catalyst for Hydrogen Evolution. *Adv. Funct. Mater.* **2013**, *23*, 5326–5333.
(27) Li, D. J.; Maiti, U. N.; Lim, J.; Choi, D. S.; Lee, W. J.; Oh, Y.; Lee, G. Y.; Kim, S. O. Molybdenum Sulfide/N-Doped CNT Forest Hybrid Catalysts for High-Performance Hydrogen Evolution Reaction. *Nano Lett.* **2014**, *14*, 1228–1233.
(28) Zhang, K.; Zhao, Y.; Zhang, S.; Yu, H.; Chen, Y.; Gao, P.; Zhu, C. MoS_2 Nanosheet/Mo_2C-

Embedded N-Doped Carbon Nanotubes: Synthesis and Electrocatalytic Hydrogen Evolution Performance. *J. Mater. Chem. A* **2014**, *2*, 18715–18719.
(29) Zheng, X.; Xu, J.; Yan, K.; Wang, H.; Wang, Z.; Yang, S. Space-Confined Growth of MoS_2 Nanosheets within Graphite: The Layered Hybrid of MoS_2 and Graphene as an Active Catalyst for Hydrogen Evolution Reaction. *Chem. Mater.* **2014**, *26*, 2344–2353.
(30) Shi, Y.; Wang, J.; Wang, C.; Zhai, T.-T.; Bao, W.-J.; Xu, J.-J.; Xia, X.-H.; Chen, H.-Y. Hot Electron of Au Nanorods Activates the Electrocatalysis of Hydrogen Evolution on MoS_2 Nanosheets. *J. Am. Chem. Soc.* **2015**, *137*, 7365−7370.
(31) Gao, M.-R.; Liang, J.-X.; Zheng, Y.-R.; Xu, Y.-F.; Jiang, J.; Gao, Q.; Li, J.; Yu, S.-H. An Efficient Molybdenum Disulfide/Cobalt Diselenide Hybrid Catalyst for Electrochemical Hydrogen Generation. *Nat. Commun.* **2015**, *6*, 5982.
(32) Liu, A.; Zhao, L.; Zhang, J.; Lin, L.; Wu, H. Solvent-Assisted Oxygen Incorporation of Vertically Aligned MoS_2 Ultrathin Nanosheets Decorated on Reduced Graphene Oxide for Improved Electrocatalytic Hydrogen Evolution. *ACS Appl. Mater. Interfaces* **2016**, *8*, 25210−25218.
(33) Zeng, Z.; Yin, Z.; Huang, X.; Li, H.; He, Q.; Lu, G.; Boey, F.; Zhang, H. Single-Layer Semiconducting Nanosheets: High-Yield Preparation and Device Fabrication. *Angew. Chem. Int. Ed.* **2011**, *50*, 11093–11097.
(34) Yan, Y.; Xia, B.; Li, N.; Xu, Z.; Fisher, A.; Wang, X. Vertically Oriented MoS_2 and WS_2 Nanosheets Directly Grown on Carbon Cloth as Efficient and Stable 3-Dimensional Hydrogen-Evolving Cathodes. *J. Mater. Chem. A* **2015**, *3*, 131–135.
(35) Lee, Y.-H.; Zhang, X.-Q.; Zhang, W.; Chang, M.-T.; Lin, C.-T.; Chang, K.-D.; Yu, Y.-C.; Wang, J. T.-W.; Chang, C.-S.; Li, L.-J.; Lin, T.-W. Synthesis of Large-Area MoS_2 Atomic Layers with Chemical Vapor Deposition. *Adv. Mater.* **2012**, *24*, 2320–2325.
(36) Wang, X.; Feng, H.; Wu, Y.; Jiao, L. Controlled Synthesis of Highly Crystalline MoS_2 Flakes by Chemical Vapor Deposition. *J. Am. Chem. Soc.* **2013**, 135, 5304–5307.
(37) Wang, S.; Rong, Y.; Fan, Y.; Pacios, M.; Bhaskaran, H.; He, K.; Warner, J. H. Shape Evolution of Monolayer MoS_2 Crystals Grown by Chemical Vapor Deposition. *Chem. Mater.* **2014**, 26, 6371–6379.
(38) Kibsgaard, J.; Chen, Z.; Reinecke, B. N.; Jaramillo, T. F. Engineering the Surface Structure of MoS_2 to Preferentially Expose Active Edge Sites for Electrocatalysis. *Nat. Mater.* **2012**, *11*, 963–969.
(39) Kong, D.; Wang, H.; Cha, J. J.; Pasta, M.; Koski, K. J.; Yao, J.; Cui, Y. Synthesis of MoS_2 and $MoSe_2$ Films with Vertically Aligned Layers. *Nano Lett.* **2013**, *13*, 1341–1347.
(40) Yang, Y.; Fei, H.; Ruan, G.; Xiang, C.; Tour, J. M. Edge-Oriented MoS_2 Nanoporous Films as Flexible Electrodes for Hydrogen Evolution Reactions and Supercapacitor Devices. *Adv. Mater.* **2014**, *26*, 8163–8168.
(41) Zhang, Y.; Ji, Q.; Han, G.-F.; Ju, J.; Shi, J.; Ma, D.; Sun, J.; Zhang, Y.; Li, M.; Lang, X.-Y.; Zhang, Y; Liu, Z. Dendritic, Transferable, Strictly Monolayer MoS_2 Flakes Synthesized on $SrTiO_3$ Single Crystals for Efficient Electrocatalytic Applications. *ACS Nano* **2014**, *8*, 8617–8624.
(42) Shi, J.; Ma, D.; Han, G.-F.; Zhang, Y.; Ji, Q.; Gao, T.; Sun, J.; Song, X.; Li, C.; Zhang, Y.; Lang, X.-Y.; Zhang, Y.; Liu, Z. Controllable Growth and Transfer of Monolayer MoS_2 on Au Foils and Its Potential Application in Hydrogen Evolution Reaction. *ACS Nano* **2014**, *8*, 10196–10204.
(43) Cao, Y.; Luo, X.; Han, S.; Yuan, C.; Yang, Y.; Li, Q.; Yu, T.; Ye, S. Influences of Carrier

Gas Flow Rate on the Morphologies of MoS_2 Flakes. *Chem. Phys. Lett.* **2015**, *631*, 30–33.
(44) Wan, W.; Zhan, L.; Xu, B.; Zhao, F.; Zhu, Z.; Zhou, Y.; Yang, Z.; Shih, T.; Cai, W. Temperature-Related Morphological Evolution of MoS_2 Domains on Graphene and Electron Transfer within Heterostructures. *Small* **2017**, *13*, 1603549.
(45) Liu, H.; Zhu, Y.; Meng, Q.; Lu, X.; Kong, S.; Huang, Z.; Jiang, P.; Bao, X. Role of the Carrier Gas Flow Rate in Monolayer MoS_2 Growth by Modified Chemical Vapor Deposition. *Nano Res.* **2017**, *10*, 643–651.
(46) Mak, K. F.; Lee, C.; Hone, J.; Shan, J.; Heinz, T. F. Atomically Thin MoS_2: A New Direct-Gap Semiconductor. *Phys. Rev. Lett.* **2010**, *105*, 136805.
(47) Van Der Zande, A. M.; Huang, P. Y.; Chenet, D. A.; Berkelbach, T. C.; You, Y.; Lee, G.-H.; Heinz, T. F.; Reichman, D. R.; Muller, D. A.; Hone, J. C. Grains and Grain Boundaries in Highly Crystalline Monolayer Molybdenum Disulphide. *Nat. Mater.* **2013**, *12*, 554–561.
(48) Foroutan-pour, K.; Dutilleul, P.; Smith, D. L. Advances in the Implementation of the Box-Counting Method of Fractal Dimension Estimation. *Appl. Math. Comput.* **1999**, *105*, 195–210.
(49) Zhang, Z.; Lagally, M. G. Atomistic Processes in the Early Stages of Thin-Film Growth. *Science* **1997**, *276*, 377–383.
(50) Zhang, Y.; Ji, Q.; Wen, J.; Li, J.; Li, C.; Shi, J.; Zhou, X.; Shi, K.; Chen, H.; Li, Y.; Deng, S.; Xu, N.; Liu, Z.; Zhang, Y. Monolayer MoS_2 Dendrites on a Symmetry-Disparate $SrTiO_3$ (001) Substrate: Formation Mechanism and Interface Interaction. *Adv. Funct. Mater.* **2016**, *26*, 3299–3305.
(51) Meakin, P. Diffusion-Limited Surface Deposition in the Limit of Large Anisotropy. *Phys. Rev. A* **1986**, *33*, 1984–1989.
(52) Robertson, A. W.; Lin, Y.-C.; Wang, S.; Sawada, H.; Allen, C. S.; Chen, Q.; Lee, S.; Lee, G.-D.; Lee, J.; Han, S.; Yoon, E.; Kirkland, A. I.; Kim, H.; Suenaga, K.; Warner, J. H. Atomic Structure and Spectroscopy of Single Metal (Cr, V) Substitutional Dopants in Monolayer MoS_2. *ACS Nano* **2016**, *10*, 10227–10236.
(53) Hansen, L. P.; Ramasse, Q. M.; Kisielowski, C.; Brorson, M.; Johnson, E.; Topsøe, H.; Helveg, S. Atomic-Scale Edge Structures on Industrial-Style MoS_2 Nanocatalysts. *Angew. Chem. Int. Ed.* **2011**, *50*, 10153–10156.
(54) Lee, C.; Yan, H.; Brus, L. E.; Heinz, T. F.; Hone, J.; Ryu, S. Anomalous Lattice Vibrations of Single- and Few-Layer MoS_2. *ACS Nano* **2010**, *4*, 2695–2700.
(55) Splendiani, A.; Sun, L.; Zhang, Y.; Li, T.; Kim, J.; Chim, C.-Y.; Galli, G.; Wang, F. Emerging Photoluminescence in Monolayer MoS_2. *Nano Lett.* **2010**, *10*, 1271–1275.
(56) Liu, Z.; Amani, M.; Najmaei, S.; Xu, Q.; Zou, X.; Zhou, W.; Yu, T.; Qiu, C.; Birdwell, A. G.; Crowne, F. J.; Vajtai, R.; Yakobson, B. I.; Xia, Z.; Dubey, M.; Ajayan, P. M.; Lou, J. Strain and Structure Heterogeneity in MoS_2 Atomic Layers Grown by Chemical Vapour Deposition. *Nat. Commun.* **2014**, *5*, 5246.
(57) Wang, S.; Wang, X.; Warner, J. H. All Chemical Vapor Deposition Growth of MoS_2:h-BN Vertical van der Waals Heterostructures. *ACS Nano* **2015**, *9*, 5246–5254.
(58) He, K.; Poole, C.; Mak, K. F.; Shan, J. Experimental Demonstration of Continuous Electronic Structure Tuning *via* Strain in Atomically Thin MoS_2. *Nano Lett.* **2013**, *13*, 2931–2936.
(59) Qiu, H.; Xu, T.; Wang, Z.; Ren, W.; Nan, H.; Ni, Z.; Chen, Q.; Yuan, S.; Miao, F.; Song, F.; Long, G.; Shi, Y.; Sun, L.; Wang, J.; Wang, X. Hopping Transport through Defect-Induced Localized States in Molybdenum Disulphide. *Nat. Commun.* **2013**, *4*, 2642.

(60) Mohsin, A.; Liu, L.; Liu, P.; Deng, W.; Ivanov, I. N.; Li, G.; Dyck, O. E.; Duscher, G.; Dunlap, J. R.; Xiao, K.; Gu, G. Synthesis of Millimeter-Size Hexagon-Shaped Graphene Single Crystals on Resolidified Copper. *ACS Nano* **2013**, *7*, 8924–8931.
(61) Wang, S.; Qin, Z.; Jung, G. S.; Martin-Martinez, F. J.; Zhang, K.; Buehler, M. J.; Warner, J. H. Atomically Sharp Crack Tips in Monolayer MoS_2 and Their Enhanced Toughness by Vacancy Defects. *ACS Nano* **2016**, *10*, 9831–9839.
(62) Trasatti, S. Work Function, Electronegativity, and Electrochemical Behaviour of Metals: III. Electrolytic Hydrogen Evolution in Acid Solutions. *J. Electroanal. Chem. Interfacial Electrochem.* **1972**, *39*, 163–184.
(63) Wu, Z.; Fang, B.; Wang, Z.; Wang, C.; Liu, Z.; Liu, F.; Wang, W.; Alfantazi, A.; Wang, D.; Wilkinson, D. P. MoS_2 Nanosheets: A Designed Structure with High Active Site Density for the Hydrogen Evolution Reaction. *ACS Catal.* **2013**, *3*, 2101–2107.
(64) Lu, Z.; Zhang, H.; Zhu, W.; Yu, X.; Kuang, Y.; Chang, Z.; Lei, X.; Sun, X. *In Situ* Fabrication of Porous MoS_2 Thin-Films as High-Performance Catalysts for Electrochemical Hydrogen Evolution. *Chem. Commun.* **2013**, *49*, 7516–7518.
(65) Zhang, J.; Liu, S.; Liang, H.; Dong, R.; Feng, X. Hierarchical Transition-Metal Dichalcogenide Nanosheets for Enhanced Electrocatalytic Hydrogen Evolution. *Adv. Mater.* **2015**, *27*, 7426–7431.
(66) Gao, M.-R., Chan, M. K. Y.; Sun, Y. Edge-Terminated Molybdenum Disulfide with a 9.4-Å Interlayer Spacing for Electrochemical Hydrogen Production. *Nat. Commun.* **2015**, *6*, 7493.
(67) Benson, J.; Li, M.; Wang, S.; Wang, P.; Papakonstantinou, P. Electrocatalytic Hydrogen Evolution Reaction on Edges of a Few Layer Molybdenum Disulfide Nanodots. *ACS Appl. Mater. Interfaces* **2015**, *7*, 14113–14122.
(68) Huang, H.; Huang, J.; Liu, W.; Fang, Y.; Liu, Y. Ultradispersed and Single-Layered MoS_2 Nanoflakes Strongly Coupled with Graphene: An Optimized Structure with High Kinetics for the Hydrogen Evolution Reaction. *ACS Appl. Mater. Interfaces* **2017**, *9*, 39380–39390.
(69) Nagasubramanian, G. Two- and Three-Electrode Impedance Studies on 18650 Li-Ion Cells. *J. Power Sources* **2000**, *87*, 226–229.

TOC FIGURE

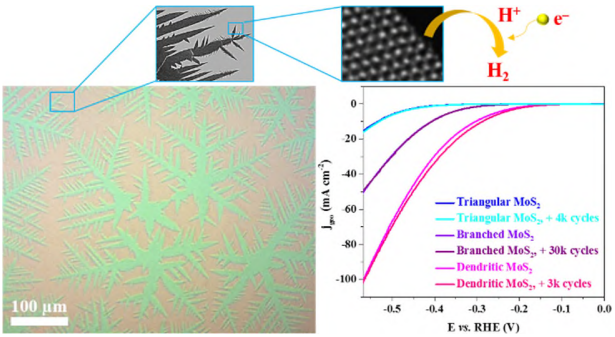
H+
e−
H2
100 μm
0
-20
-40
-60
-80
-100
-0.5
-0.4
-0.3
-0.2
-0.1
0.0
E vs. RHE (V)
Triangular MoS2
Triangular MoS2 + 4k cycles
Branched MoS2
Branched MoS2 + 30k cycles
Dendritic MoS2
Dendritic MoS2 + 3k cycles